Lawrence Berkeley National Laboratory

Title
Laser induced plasma diagnostics of pulsed laser ablation in a cavity

Permalink
https://escholarship.org/uc/item/6z56d9f1

Journal
Spectrochimica Acta Part B: Atomic Spectroscopy, 58(5)

Authors
Zeng, Xianzhong
Mao, Samuel S.
Liu, Chunyi
et al.

Publication Date
2002-10-01

Laser induced plasma diagnostics of pulsed laser ablation in a cavity

Xianzhong Zeng, Samuel S. Mao, Chunyi Liu, Xianglei Mao, Ralph Greif, Richard E. Russo*

Lawrence Berkeley National Laboratory, Berkeley, CA 94720

*corresponding author

Abstract

The formation of a laser-induced plasma in a cavity and the effects of a cavity on the ablation process were investigated. Cavities were fabricated in fused silica with equal depths and variable diameters to provide aspect ratios (depth/diameter) of 1, 3 and 6. The temperature and electron number density of the pulsed laser induced plasma in the cavities were determined from spectroscopic measurements. Reflection and confinement effects by the cavity walls and plasma shielding were discussed to explain increased temperature and electron number density with increasing cavity aspect ratio. The temporal variations of the plasma temperature and electron number density sharply decreased inside the cavity. An adiabatic expansion model was not suitable for the laser-induced plasma in the cavity because plasma wall interactions were not included. Properties of laser-induced plasmas in the cavities and on a flat surface were compared.

Keywords: Laser ablation, Cavity structure, Laser-induced plasma, Cavity aspect ratio

1. Introduction

Depending on the laser intensity, laser ablation of solids involves processes of heating, melting, vaporization, ejection of atoms, ions and molecules, shock waves, plasma initiation and plasma expansion. The amount of laser energy coupled into a material influences the amount of mass removed, its temperature, phase, and degree of ionization [1]. Many laser–material processes produce cavity structures; e.g. laser drilling, micromachining, and depth resolved chemical analysis [2, 3, 4]. Laser beam energy coupling to a solid was found to increase as a cavity was formed in a target [5, 6]. The increase in energy coupling was related to the cavity depth-to-diameter (aspect) ratio. For an aspect ratio varying from 0 to 5, the amount of energy coupled increased approx 10 times compared to the energy coupled to a flat surface [5].

Elemental depth variations in solid samples are important for micro analytical applications; for example, analysis of inclusion spatial heterogeneity, and elemental diffusion. Previous work [7, 8, 9] showed that the cavity aspect ratio influenced elemental fractionation, a process during which elements are selectively ablated; the ablated mass composition is not the same as the solid. For some elements, fractionation became significant when the cavity aspect ratio was greater than six [7]. Mechanisms to describe the effect of the cavity aspect ratio on fractionation have not been established. Because the plasma is restricted in the cavity at early times, it may have a larger electron number density and be at a higher temperature compared to a plasma produced at a flat surface. At higher temperatures, the plasma can transfer heat more effectively to the cavity walls. Low melting/vaporization point elements may be selectively removed from the sample by

a plasma heating process [7]. As the aspect ratio increases, plasma heating may become the dominant sampling process.

In this work, plasma properties were measured inside and outside of prefabricated cavities in fused silica samples. The spatial distribution (up to 1 mm above the target surface) of the plasma temperature and electron number density were determined by measuring the Stark broadening of the Si emission lines and the relative line-continuum ratio at times from 60 to 300 ns after the laser pulse.

2. Experimental system

A diagram of the experimental system can be found in ref. [10]. A 266 nm Nd:YAG laser (Coherent, Infinity) with a 3-ns pulse width was used as the ablation laser. The laser beam was focused vertically onto the sample with a quartz lens to a spot diameter of ~50 microns in air at 1 atm. pressure. The pulse energy was measured using a pyroelectric detector and a joulemeter. A second lens was used to image the laser-induced plasma horizontally onto the entrance slit of a Czerny-Turner spectrometer (Spex Industries Model 270M). Spectral emission was detected by an Intensified Charge-Coupled Device (ICCD) system which consists of a thermoelectrically cooled CCD (EG&G Princeton Applied Research Model OMA VISION) with 512×512 pixels and a Microchannel Plate (MCP) image intensifier. This detection system provides a spectral window of ~13 nm and resolution of typically 0.125 nm, using an entrance slit width of 20 micron and grating of 1800 grooves/mm. The spatial resolution of the ICCD spectrometer plus lens

arrangements was 11 microns per pixel. The dark current background of the CCD detector was subtracted from the measured spectroscopic data for each measurement.

Gating the ICCD and changing the delay time enables the spectra to be temporally resolved. The gate width and time delay were controlled by the OMA SPEC 4000 software (EG&G Princeton Applied Research), and synchronously triggered from the Nd:YAG laser. A photo diode and a digitizing oscilloscope were used to calibrate the time delay. The gate width was set at 30 ns.

Fused silica was cut into samples of 2 mm width and 2 mm height, and placed on an *xyz* translation stage. Cavities were pre-fabricated using using Gaussian beam nanosecond laser ablation, by varying the lens-to-sample distance (spot size), energy, and number of pulses. Three cavities with the same depth of about 0.5 mm, and different diameters were obtained by repetitive laser ablation to produce aspect ratios of 1, 3 and 6 (Fig. 1). A white-light interferometric microscope (New View 200, Zygo Corporation) and CCD camera system were used to measure the cavity dimensions. All three cavities narrowed towards the bottom, and cavity walls were not smooth due to fracturing. Single pulse laser ablation was performed at the bottom surface of these cavities. The plasma properties measured in the cavities were compared to those from ablation at the flat sample surface. The spot size and energy (fluence) were equal when the laser beam was incident on the flat surface and on the bottom surface of each cavity.

4

3. Results and discussion

Spectral line analysis

The silicon emission line Si(I) at 288.16 nm was measured for diagnosing plasma properties. Fig. 2a shows the spectra from single pulse laser ablation inside a cavity of 160-micron diameter at 100 ns time delay. The plasma spectra from ablation on a flat surface using the same laser conditions are shown in Fig. 2b. Inside the cavity, the spectra have a wider Full Width at Half Maximum (FWHM) and greater emission intensity. The maximum emission intensity from the cavity plasma occurs 0.9 mm above the cavity bottom (0.5 mm depth). The location of maximum emission intensity occurred at 0.6 mm above the flat surface.

Stark line broadening from collisions of charged species is the primary mechanism influencing these emission spectra. The Lorentz function can be used to fit these spectra and is expressed as [10]:

$$y = y_0 + \frac{2A}{\pi} \frac{w}{4(x - x_c)^2 + w^2} \tag{1}$$

where w is the full width at half maximum, x_c is the center wavelength, y_0 is the background emission, and A is the integrated area of the emission line. The values of these parameters were obtained by fitting the spectral lines (as shown in Fig. 3) and were used to deduce the electron number density and temperature of the plasmas.

Other contributions to spectral line broadening were considered. Doppler broadening due to the random thermal motion of the emitters was estimated by using

5

$w_{1/2} = 7.16 \times 10^{-7} \lambda (T/M)^{1/2}$, where M is the atomic weight, T is the plasma temperature

in Kelvin, and λ is the line wavelength [11]. As will be shown below, the calculated

highest plasma temperature was less than 60,000 K. The calculated Doppler effect will

cause a change in line-width for Si(I) 288.16 nm of less than 0.01 nm. Compared with the

total line widths (usually about 1 nm), the Doppler effect can be ignored. Resonance

broadening is neglected since the atomic Si(I) 288.16 nm line is not a resonance

transition [10].

Electron number densities

The FWHM of Stark broadened lines is related to the electron number density n_e by the

expression [12]:

$$\Delta\lambda_{1/2} = 2W \left(\frac{n_e}{10^{16}} \right) \left[1 + 1.75A \left(\frac{n_e}{10^{16}} \right)^{1/4} \left(1 - \frac{3}{4} N_D^{-1/3} \right) \right] \tag{2}$$

where N_D is the number of particles in the Debye sphere and is estimated from:

$$N_D = 1.72 \times 10^9 \frac{T^{3/2}}{n_e^{1/2}} \tag{3}$$

where T is in eV and n_e is in cm^{-3}.

Plasma temperature

Under the assumption of local thermal equilibrium (LTE), the electron temperature T_e can

be assumed equal to the excitation temperature T_{exc}, namely $T_e = T_{exc} = T$. Therefore, the

plasma temperature T can be determined by the relative line-to-continuum intensity ratio

using the following equation [13]:

$$\frac{\varepsilon_l}{\varepsilon_c}(\lambda) = C_r \frac{A_{21}g_2}{Z_i} \frac{\lambda_c^2}{\lambda_l T_e} \frac{\exp\left(\frac{E_i - E_2 - \Delta E_i}{kT_e}\right)}{\left[\xi\left(1 - \exp\frac{-hc}{\lambda kT_e}\right) + G\left(\exp\frac{-hc}{\lambda kT_e}\right)\right]} \tag{4}$$

where ε_c is the continuum emission coefficient and ε_l is the integrated emission coefficient over the line spectral profile. The ratio $\varepsilon_c/\varepsilon_l$ can be calculated from the integrated line intensity and continuum intensity at certain adjacent wavelength positions. λ_c, λ_l are the continuum and center wavelength of the spectral line, respectively. By using a Lorentz fit, the position was obtained, so $\lambda_l = \lambda_c$. Z_i is the partition function for ions, and must be calculated as a function of temperature. A_{21} is the Einstein transition probability of spontaneous emission, and E_i is the ionization potential. E_2 and g_2 are upper level energy and degeneracy, respectively. ΔE_i is the lowering of the ionization potential of atoms in the presence of a field of ions and is small enough to be neglected. G is the free-free Gaunt factor, and ξ is the free-bound continuum correction factor. The parameters used for T_e and n_e are listed in Table 1 [14, 15].

The partition function is given by [16]:

$$Z(T) = \sum_i g_i \exp\left(-\frac{E_i}{kT}\right) \tag{5}$$

where g_i is the degeneracy or statistical weight of the i-th energy level E_i.

$$g_i = 2J_i + 1 \tag{6}$$

and J_i is the angular momentum quantum number of the level. E_i and J_i values were obtained from the NIST data bank [17]. The partition function of singly-charged silicon

(7)

ions was calculated for the temperature interval from 6,000 to 60,000 K and was approximated by a fifth-order polynomial:

$$Z(T) = 5.33707 + 1.05984Y - 0.87284Y^2 + 0.32479Y^3 + 0.02802Y^4 - 0.00578Y^5$$

where $Y = T \times 10^{-4}$ K. The calculated partition function values agree with those reported in ref. 18 to within 0.5% for temperatures between 6000 and 12000 K (greatest temperature range available in literatures).

The lower limit for the electron number density needed to collisionally maintain the energy-level populations to within 10% of LTE while competing with radiative decay is [10, 19, 20]:

$$n_e(cm^{-3}) \geq 1.4 \times 10^{14} (kT)^{1/2} \Delta E^3 \qquad (8)$$

where T is the temperature and ΔE is the energy difference between the upper and lower states. For the Si(I) transition at 288.16 nm, $\Delta E = 4.3$ eV, and at the highest temperature $kT = 4.9$ eV, the lower limit for n_e is 2.5×10^{16} cm^{-3}, which is approximately two orders of magnitude lower than the value of n_e deduced from Stark broadening. Therefore, the validity of the LTE assumption is supported.

Using the Saha equation and the calculated electron number density, the first ionization level of Si will be dominant when the plasma temperature is less than 2.5 eV. When the plasma temperature is greater, ionization will shift toward higher levels and electron collisions with higher ionization states will contribute to continuum radiation, the temperature calculated from Eq. (4) may be greater than the accurate plasma temperature.

Effect of aspect ratio

Single pulse ablation was performed in the three cavities and at the flat surface of the sample; data are shown in Fig. 4a (plasma temperature) and Fig. 4b (electron number density) for a delay time of 100 ns. The plasma temperature and electron number density are greatest in the largest aspect-ratio cavity. As the aspect ratio decreases, the plasma temperature and electron number density in the cavity approach the flat surface condition. For the largest aspect ratio, the plasma temperature decreases from 38000 K (in the cavity) to 30000 K (1.5 mm above the cavity bottom); electron number density falls from 2×10^{19} to 5×10^{18} cm^{-3}. On a flat surface, the plasma temperature and electron number density are much lower, 20000 K and 2×10^{18} cm^{-3}, respectively, and do not change as much with distance from the surface.

Overall, the temperature and electron number density are greater for laser ablation in a cavity compared to flat surface ablation. Comparing the data at 0.2mm above the cavity bottom with the data at 0.2mm above flat surface, n_e is ~10X and T is only ~2X in the cavity with aspect ratio of 6. These results are believed to be related to reflection and confinement effects by the cavity walls and plasma shielding (absorption and/or reflection of the laser beam by the plasma). Once the plasma is initiated in the cavity, its lateral expansion is confined; electron number density increases greatly, leading to enhanced absorbing of the trailing part of the laser pulse. Additional electrons will be produced via electron-neutral, electron-ion inverse bremsstrahlung, and photoionization [21]. The absorbed energy is converted into internal energy of the plasma. Since the plasma temperature is much higher than the surrounding wall temperature, its internal

energy decreases quickly by radiation and other methods. Thus, at 100 ns, plasma temperature is only ~2X in the cavity compared with ~10X electron number density. Increased plasma temperature and electron number density in cavities has been reported [8, 9]. Jeong, et al. [6] reported an increase in coupled laser-beam energy by multiple-reflections of the cavity walls utilizing a photothermal deflection measurement technique. Shannon's [5] radiative cavity analysis demonstrated that energy coupling in a cavity increased with increasing aspect ratio, consistent with the data measured here.

3.4 Temporal evolution

Figures 5a and 5b show the spatial plasma temperature and electron number density inside and outside of a cavity and for the flat surface at three different times, 100, 150 and 265 ns. Both plasma temperature and electron number density are higher inside the cavity than outside the cavity at times of 100 and 150 ns. However, at 265 ns, the electron number density inside the cavity drops below the value outside the cavity, and the plasma temperature inside the cavity approaches the plasma temperature outside the cavity. The plasma temperature and electron number density decrease with time for both the cavity and flat surface. However, the plasma temperature and electron number density in the cavity decrease at a faster rate than for the plasma outside of the cavity and on the flat surface, especially during early times ($t = 100{\sim}150$ ns).

To compare the temporal evolution of the plasmas, we selected two locations for the cavity and one location for the flat surface (Figures 6a and 6b). Location A is inside the cavity at a height 0.2 mm above the bottom surface, location B is outside of the cavity at

a height 0.7 mm above the bottom of the cavity. Location C is 0.2 mm above the flat surface. Location A and C are equal distance above solid material.

The plasma temperature and electron number density in the cavity at location A are higher than both outside the cavity at location B and for the flat surface at location C. Plasma temperature and electron number density in the cavity (A) decrease faster than both outside of the cavity (B) and from the flat surface (C). As the plasma expands there is a sharp decrease of the temperature and electron number density inside the cavity at A. Outside of the cavity, the temperature and electron number density at B decrease at a similar rate to the plasma from the flat surface generated at C.

An adiabatic model is often used to describe laser-induced plasma expansion [21, 22, 23]. For an adiabatic expansion, the expressions for plasma temperature and electron number density as a function of time are: [10, 21]

$$T(t) \propto t^{-2\alpha(\gamma-1)/[\alpha(\gamma-1)+2]}, \quad n_e(t) \propto t^{-2\alpha/[\alpha(\gamma-1)+2]} \tag{9}$$

where γ is the ratio of specific heat capacities at constant pressure to constant volume, and α is the flow dimensionality: $1<\alpha<3$ [21, 22, 23].

.

The plasma at location C from laser ablation on the flat surface gives:

$$T \propto t^{-0.54\pm0.04}, \quad n_e \propto t^{-0.95\pm0.06} \tag{10}$$

Solving for α and γ yields:

$$\alpha = 1.30\pm0.12, \quad \gamma = 1.57\pm0.08 \tag{11}$$

The calculated values of α and γ are within experimental error to the values obtained by Liu, et al. [10]. The calculated dimensionality 1.30 supports preferential spatial expansion in the direction perpendicular to the target [21, 22, 23]. The calculated γ value, 1.57 is close to the specific heat for an ideal gas of 5/3. Therefore, an adiabatic process can be used to describe the plasma expansion for this experiment.

Plasma expansion outside the cavity at location B gives:

$$T \propto t^{-0.52\pm0.03}, n_e \propto t^{-0.98\pm0.05} \tag{12}$$

From equations (9) and (12),

$$\alpha = 1.32\pm0.09, \gamma = 1.53\pm0.06 \tag{13}$$

which are close to the flat surface results above. Thus, after the plasma expands out of the cavity, an adiabatic model can describe plasma temperature and electron number density variations.

For the plasma in the cavity at A,

$$T \propto t^{-1.08\pm0.04}, n_e \propto t^{-1.51\pm0.06} \tag{14}$$

Therefore,

$$\alpha = 3.31\pm0.17, \gamma = 1.72\pm0.05 \tag{15}$$

The dimensionality value is greater than 3 (3-Dimension expansion), which indicates that an adiabatic expansion model is not suitable for the laser-induced plasma in a cavity. To describe the processes of a laser-induced plasma in cavity and account for the sharp decrease of plasma temperature and electron number density (cf. Figures 6a, 6b), plasma wall interactions should be included in the expansion model analysis. Energy from the

plasma can be transferred to the wall by any of the four mechanisms: (1) normal electron heat conduction, (2) electron-ion (exothermic) recombination on the cavity walls, (3) short-wavelength thermal plasma radiation, and (4) condensation of vapor that moves to the surface due to the plasma pressure [2].

4. Conclusions

The formation of a laser-induced plasma inside a cavity and the cavity effects on plasma expansion were investigated. The temperature and electron number density of a laser-induced plasma inside a cavity were greater than outside of a cavity. When the aspect ratio was six, the plasma temperature inside the cavity was twice that for flat surface ablation and the electron number density was a factor of 10X greater.

As the aspect ratio decreased, the plasma temperature in the cavity approached the surface results. Plasma wall interactions must be studied to describe the plasma in the cavity and explain the sharp decrease of plasma temperature and electron number density inside the cavity. As time increased, the plasma temperature and electron number density inside the cavity decreased faster than outside of the cavity; an adiabatic model was not suitable to describe the plasma in the cavity because plasma wall interactions were not included.

5. Acknowledgments

References

[1] J.F. Ready, Effects of High-Power Laser Radiation (Academic, New York, 1971).

[2] M.V. Allmen, Laser-beam Interactions with Materials (Springer-Verlag, New York, 1987).

[3] E. N. Sobol, Phase Transformations and Ablation in Laser-Treated Solids (John Wiley & Sons, New York, 1995).

[4] L. W. Boyd, Laser Processing of Thin Films and Microstructures (Springer-Verlag, New York, 1987).

[5] M. A. Shannon, Applied Surface Science, 127-129, 218 (1998).

[6] S. H. Jeong, J. Appl. Phys. 80, 1996 (1996).

[7] A.J.G. Mank, P.D. Mason, J. Anal.At.Spectrom. 14, 1143 (1999).

[8] O.V. Borisov, X. Mao, R. E., Russo, Spectrochim. Acta Part B 55, 1693 (2000).

[9] S.M. Eggins, L.P.J. Kinsley, J.M.G. Shelley, Appl.Surf.Sci. 127-129, 278 (1998).

[10] H.C. Liu, X.L. Mao, J.H. Yoo, R.E. Russo, Spectrochim. Acta Part B 54, 1607 (1999).

[11] M. Miller, in: A. Montaser, D.W. Golightly (Eds.), Inductively Coupled Plasmas in Analytical Atomic Spectrometry (VCH Publishers Inc, New York, 1987).

[12] G. Befeki, Principles of laser plasmas (Wiley Interscience, New York, 1976).

[13] G.J. Bastiaans, R.A. Mangold, Spectrochim.Acta, Part B 40B, 885 (1985).

[14] H.R. Griem, Spectral Line Broadening by Plasmas (Academic, New York, 1974).

[15] L. Spitzer, Physics of Fully Ionized Gases (John wiley & Sons, New York, 1962).

[16] H.R. Griem, Plasma Spectroscopy (McGraw-Hill, New York, 1964).

[17] Atomic Spectra Databases. Version 2.0. National Institute of Standards and Technology (NIST), USA, 1999. (http://www.nist.gov).

[18] S. Tamaki, T. Kuroda, Spectrochimica Acta, 42B, 1105 (1987).

[19] P.J. Wolf, J.Appl.Phys. 72, 1280 (1992).

[20] R.W.P. McWhirter, in: R.H. Huddlestone and S.L. Leonard (Eds.), Plasma Diagnostic Techniques (Academic, New York, 1965).

[21] C.R. Phipps, R.W. Dreyfus, in: A. Vertes, R. Gijbels, F. Adams (Eds.), Laser Ionization Mass Analysis (John Wiley & Son, New York, 1993).

[22] R.K. Singh, J. Narayan, Phys. Rev. B 41, 8843 (1990).

[23] R.K. Singh, O.W. Holland, J. Narayan, J. Appl. Phys. 68, 233 (1998).

Figure Captions

Fig. 1. Cavities formed during repetitive laser ablation in fused silica. (a) 80-micron diameter, 480-micron depth cavity formed after 700 pulses laser ablation at an irradiance of 2.9 GW/cm^2. (b) 165-micron diameter, 485-micron depth cavity formed after 850 pulses laser ablation at an irradiance of 2.1 GW/cm^2. (c) 490-micron diameter, 480-micron depth cavity formed after 1100 pulses laser ablation at an irradiance of 1.5 GW/cm^2. The bold lines are schematic cross-sections of the cavities.

Fig. 2. (a) Spatial distributions of plasma emission from the 160-micron diameter cavity (depth 480 micron) in silica at wavelength of Si(I) 288.16 nm and time of 100 ns. Irradiance was 15.9 GW/cm^2. (b) Spatial distributions of plasma emission from the flat surface at wavelength of 288.16 nm and time of 100 ns, irradiance was 15.6 GW/cm^2.

Fig. 3. Lorentzian fitting of the Stark broadened profile for Si 288.16 nm. The full width half maximum (FWHM) was used for the calculation of the electron number density. The ratio of the integrated spectral line intensity (A) and continuum intensity (y_0) at the center wavelength (x_c) were used for the calculation of plasma temperature.

Fig. 4. (a) Plasma temperature and (b) electron number density vs. distance from surface. Compare effect of diameter at time of 100 ns and an irradiance of 6.95 GW/cm^2.

Fig. 5. (a) Temporal evolution of plasma temperature and (b) Electron number density vs. distance from surface. Compare cavity (Diameter 85 micron, depth 500 micron) and flat surface ablation results, irradiance is 7.95 GW/cm^2.

Fig. 6. (a) Temporal evolution of plasma temperature inside and outside of the cavity. (b) Temporal evolution of electron number densities inside and outside of the cavity. Cavity diameter is 80 micron and depth 480 micron. Irradiance is 7.67 GW/cm^2.

Table 1. The parameters used for plasma temperature and electron number density calculations

$A_{21}(10^8 s^{-1})$	g_2	$E_2(eV)$	$E_i(eV)$	ξ	G	$W(nm)$	A	$C_r(sK)$
1.9	3	5.028	8.151	1.4	1	0.848×10^{-3} [14]	0.027	2.005×10^{-5}

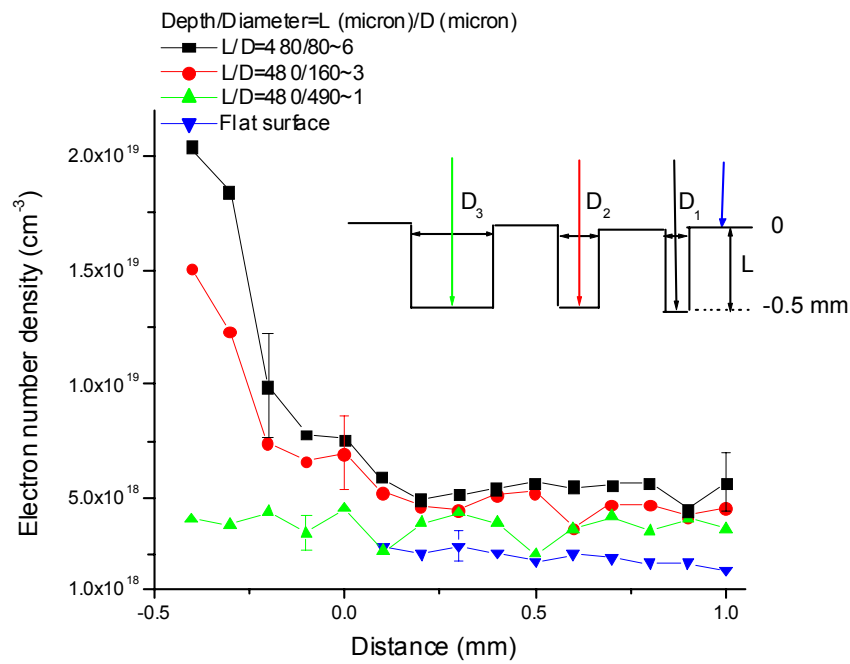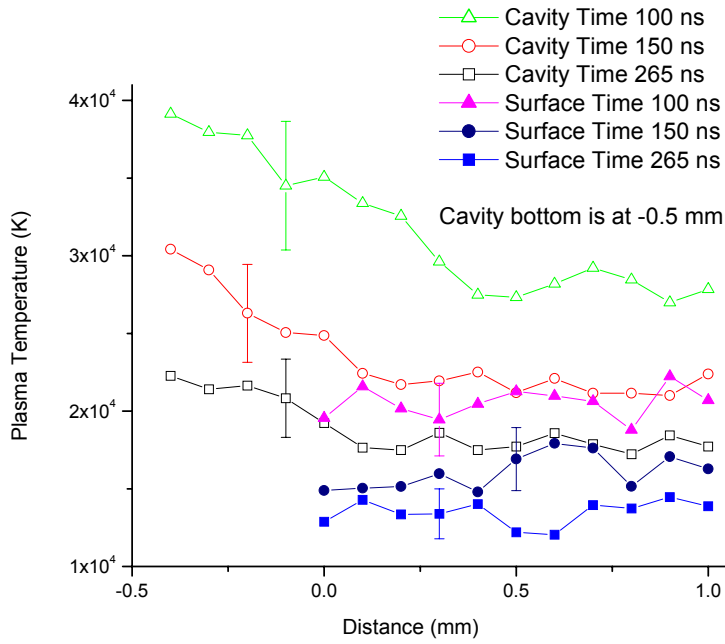80 μm   165 μm   490 μm

500 μm

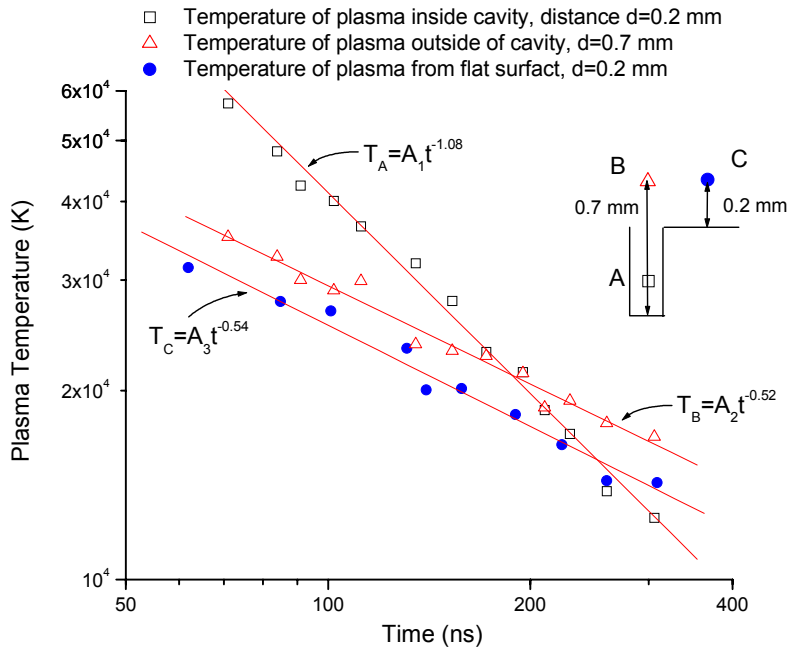(a)   (b)   (c)
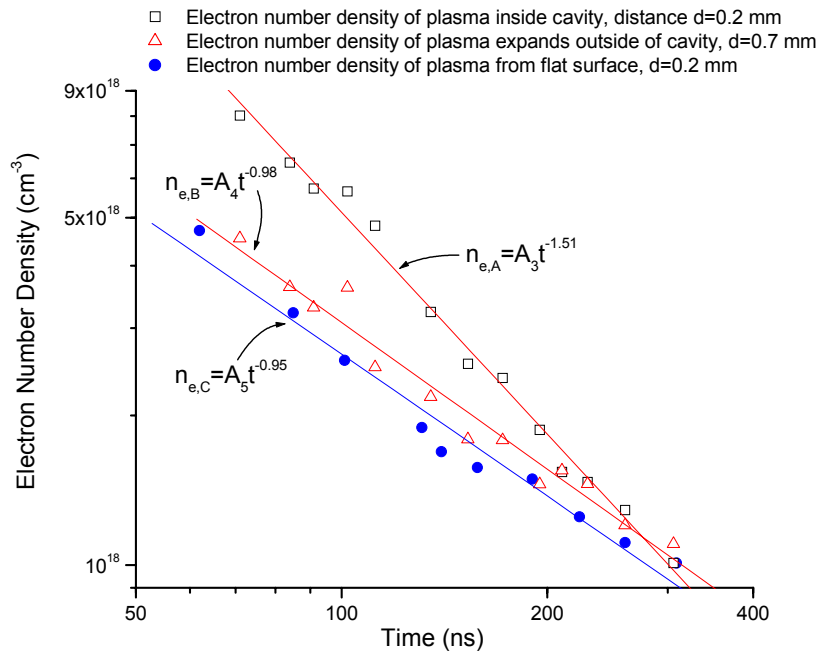
19
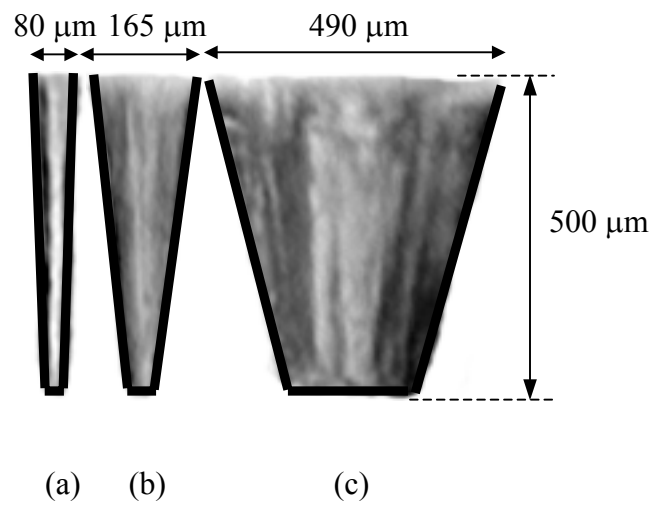
Fig. 1
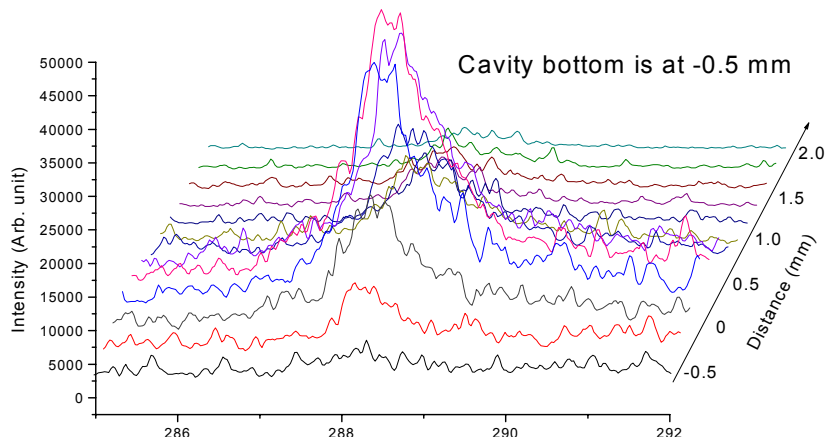
Fig. 2a
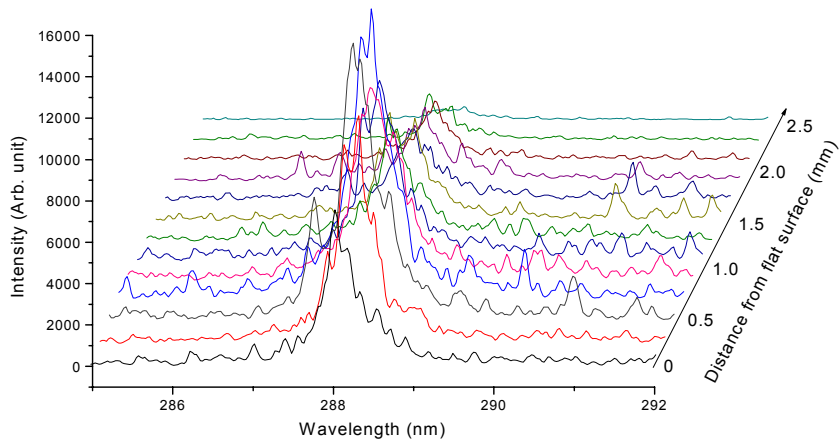
Fig. 2b
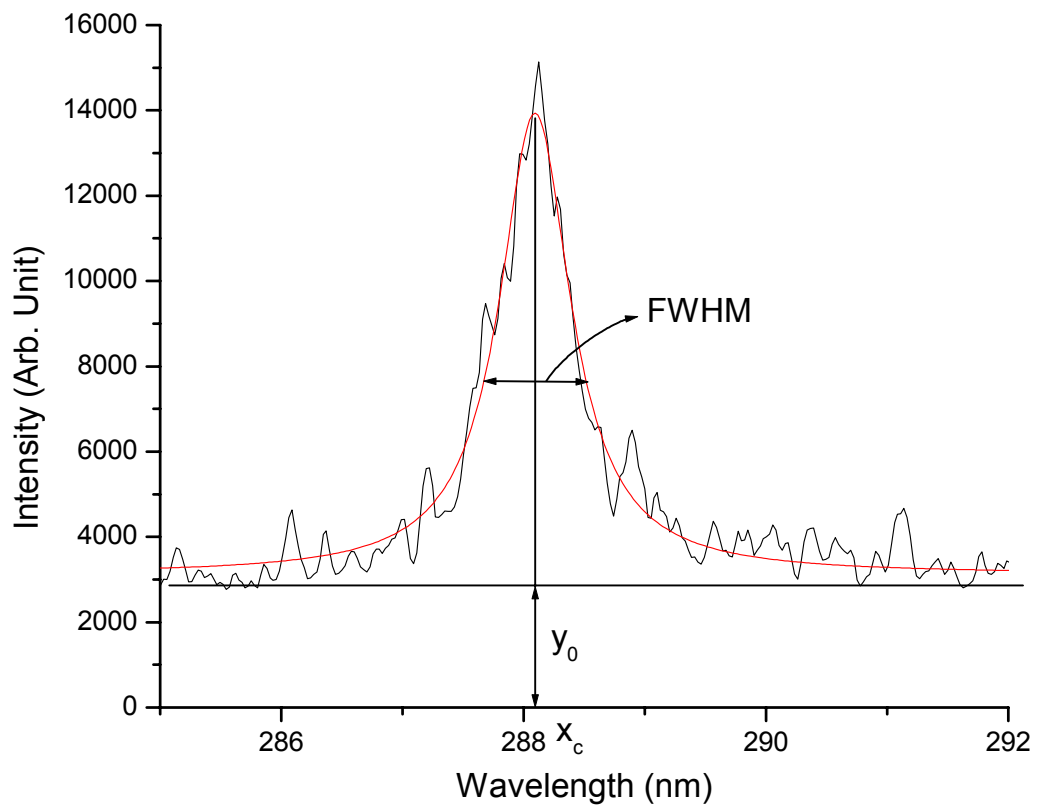
Fig. 3
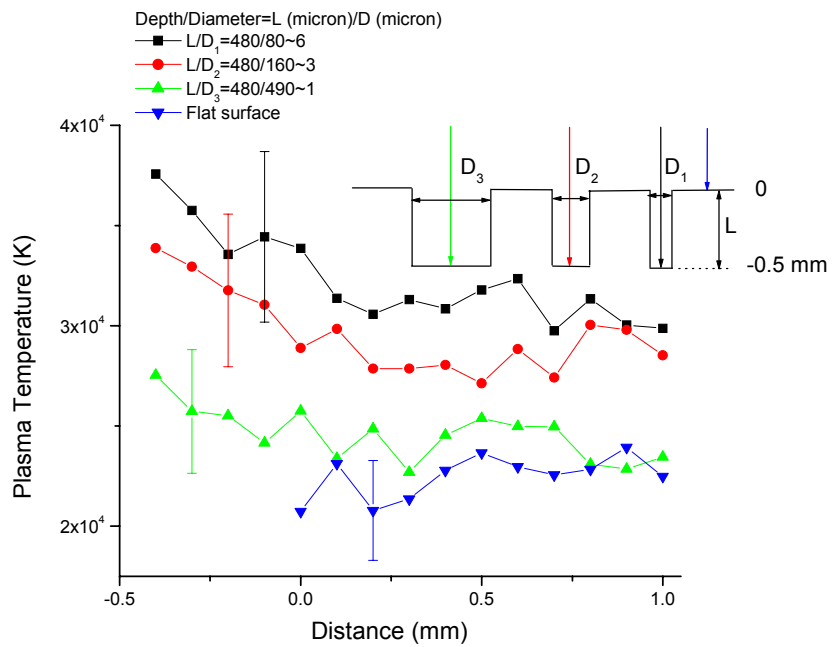
Fig. 4a

Fig. 4b

Fig. 5a

Fig. 5b

Fig. 6a

Fig. 6b